Journal of Materials Research and Technology 32 (2024) 3070–3082

Contents lists available at ScienceDirect

Journal of Materials Research and Technology

journal homepage: www.elsevier.com/locate/jmrt

# Grain refining in additively manufactured titanium using boron nitride nanosheets

A. Sola [a,b], J. Jacob [a], S.R. Kada [a,c], J. Wang [a,c], P.A. Lynch [a,c], E. Brodie [d], A. Trinchi [a,*], T.W. Turney [a,d]

[a] Commonwealth Scientific and Industrial Research Organisation (CSIRO), Manufacturing Business Unit, Clayton, Victoria, Australia
[b] University of Modena and Reggio Emilia, Department of Sciences and Methods for Engineering (DISMI), Reggio Emilia, Italy
[c] Deakin University, Institute of Frontier Materials (IFM), Waurn Ponds, Victoria, Australia
[d] Monash University, Department of Materials Science and Engineering, Clayton, Victoria, Australia

ARTICLE INFO

Handling editor: L Murr

*Keywords:*
Additive manufacturing
Powder bed fusion
Titanium
Boron
Boron nitride
Nanomaterial
Composite
Functionalization
SAXS
WAXS
XRD

ABSTRACT

The functionalization of additive manufacturing (AM) powders with nucleating particles has the potential to alter the grain structure, and hence the mechanical properties of 3D printed structures. We have investigated use of hexagonal boron nitride (BN) nanosheets to modify the microstructure of Ti parts produced by laser-based powder bed fusion (PBF-LB). The components were 3D printed from commercially pure titanium (cp-Ti) powders coated with small amounts (1.5 vol% ≈ 0.77 wt%) of BN nanosheets. As a comparison, pure cp-Ti parts were also built under the same processing conditions. Small- and wide-angle X-ray scattering (SAXS-WAXS) analysis of the 3D printed test structures revealed that BN addition significantly refined the α-Ti grain size and randomized the α-Ti texture. It was observed that grain-refined Ti-BN samples were harder and more brittle than their pure cp-Ti counterparts. This research provides new insights for grain refining using functional powder feedstocks with relatively simple powder pre-processing, and may be applied more broadly in laser-based metal AM.

## 1. Introduction

One of the challenges in metal additive manufacturing (AM) is achieving microstructural features similar to those obtained using traditional fabrication techniques. Undesirable features often arising during metal 3D printing are large grains and columnar grain structures [1]. In both cases, they pose a serious threat to the component's structural integrity, leading to poor tensile and yield strength [2].

Metal AM techniques lend themselves to very high thermal gradients and cooling rates, which results in out-of-equilibrium solidification [3]. Moreover, the layer-by-layer build-up mechanisms create significant anisotropy of the mechanical properties, with vast differences occurring in the build direction as opposed to the transverse direction [4]. During an AM build process from metal powders, grains in the melt pool will nucleate starting from the surface of the previous layer. Grains may then grow out from these nucleation sites with regular structures, such as columnar growth, adversely affecting the part's mechanical response, and thus causing hot tearing along columnar grain boundaries [5], and even causing higher risk of corrosion attack [6].

A possible way around this consists in introducing small amounts of additives that promote grain refinement. It is commonly accepted that accelerated heterogeneous nucleation requires a combination of nucleant and solute effects [7]. Nuclei that solidify at a much higher temperature than the bulk metal/alloy provide the starting point for crystallisation to occur as the melt cools down. Meanwhile, the presence of a solute may promote constitutional undercooling. If the constitutionally undercooled zone builds up quickly ahead of the solidification front, heterogeneous nucleation of the melt can be triggered promptly, thus reducing the final grain size. The ability of a solute to produce constitutional undercooling can be quantified through the growth restriction factor, $Q$, expressed as:

$$Q = m_l c_0 (k-1) \quad \text{Equation 1}$$

Where $m_l$ is the slope of the liquidus, $c_0$ is the solute concentration in

* Corresponding author.
*E-mail address:* adrian.trinchi@csiro.au (A. Trinchi).

https://doi.org/10.1016/j.jmrt.2024.08.143
Received 1 August 2024; Received in revised form 20 August 2024; Accepted 21 August 2024
Available online 22 August 2024

the melt, and $k$ is the partition coefficient [7].

Further to promoting heterogeneous nucleation within the melt pool, since 3-dimensional (3D) printed parts are generally built layer upon layer, it is then important to prevent grain growth due to re-heating as subsequent layers are being added on top of the previous ones. This can be achieved through Zener pinning by the precipitation of a thermally stable second phase at the grain boundaries [8].

Capitalising on the experience garnered with conventional powder metallurgy, different nanostructured additives or modifiers can ameliorate the microstructure of AM metal components during the build process itself without additional post-processing (e.g., post-printing thermal treatment) [9].

When it comes to titanium (Ti), boron (B) may accomplish each of these roles simultaneously [10]. Boron is extremely efficient in producing constitutional undercooling, since it has the largest growth restriction factor in Ti tabulated so far [7]. If the B concentration is locally hypereutectic, primary TiB crystals will form and act as nucleating agents for Ti. The eutectic reaction leads to the formation of TiB nanowhiskers that preferentially migrate to the Ti grain boundaries [11,12], where they avoid any further grain growth upon re-heating through Zener pinning. Thanks to the presence of B, it may be possible to favour the columnar to equiaxed (CTE) transition, promote grain refinement, and hence overcome some of the microstructural limitations that currently exist during AM processes [1].

Although the cubic form has also been used in the literature [13], hexagonal boron nitride (BN) is a convenient source of B [10]. Hexagonal BN has a melting point of 2973 °C, significantly higher than that of Ti (1668 °C). However, its high laser absorption coefficient results in BN dissolution/decomposition to B and nitrogen (N) when irradiated during laser-based AM [10]. Moreover, BN nanosheets are a plate-like 2-dimensional (2D) nanomaterial with a layered structure similar to that of graphene. Being relatively large and thin, BN nanosheets are expected to efficiently adhere to the surface of Ti particles, and to dissolve in the melt more promptly than three-dimensional bulkier BN forms would do.

Here we investigate the role that relatively small amounts (1.5 vol ≈ 0.77 wt%) of hexagonal BN nanosheets play when blended with commercially pure Ti (cp-Ti) and examine their effect on the structural and mechanical properties of parts 3D printed by laser-beam powder bed fusion (PBF-LB, aka selective laser melting, SLM). As evidenced by the characterisation results, while the addition of BN produces a refined and less textured grain structure, the full exploitation of the potential benefits of BN may be impaired by cracks and print defects being generated under unoptimized processing parameters. While the impact of adding BN on the mechanical properties (especially Vickers hardness) of the printed parts is obvious, revealing the underpinning microstructural changes that are responsible for the macroscale behaviour may be challenging, thus calling for sophisticated characterisation techniques.

## 2. Materials and methods

### 2.1. Feedstock powders

Spheroidized cp-Ti grade 1 powders (particle size range of 15–45 μm) were purchased from Carpenter Additive. Hexagonal BN (lateral size: below 1 μm; thickness: 15 nm–35 nm) was sourced from ESK Ceramics (product labelled as “Bornonid TCP001”).

Cp-Ti was pre-blended with BN by 1.5 vol% in a glove bag, then the powder mixture was ball-mixed in plastic jars together with 2.5 mm diameter zirconia balls at a powder-to-ball mass ratio of 1:2. The jars were evacuated and backfilled with argon to remove any residual atmospheric oxygen and nitrogen before sealing the lids with parafilm tape. The jars were placed on rollers and milled for 14 h at 50 rpm. After that, the zirconia balls were removed using a sieve, and the powder mixtures used for printing.

### 2.2. Additive manufacturing

The components to be printed were modelled using Autodesk (AutoCAD2020). Each build plate (90 mm × 90 mm) could accommodate two dumbbell-like blocks (envelope size: X-Y-Z: 71.5 mm × 12 mm × 15 mm each), three cylinders (diameter: 10 mm, height: 10 mm), three cubes (10 mm side), and three rods (diameter: 1 mm, height: 10 mm). Different sizes and geometries were included in order to verify the printability of the Ti-BN system and produce specimens for different characterisation techniques.

The generated .stl file was input in the slicing software AutoFab MLab (Marcam Engineering GmbH). The layer thickness was set to 25 μm. The.cls file was then exported to the PBF-LB printer. All jobs were completed on a Concept Laser Mlab R printer (GE Additive), with a 100 W Nd:YAG laser, 50 μm spot size. The printing parameters were selected through the built-in CL WRX Control 2.0 software interface (GE Additive). For comparative purposes, both materials were processed under identical conditions applying the pre-optimised parameters for cp-Ti (cl41_cusing_100_V1_ Cambridge). For each feedstock, the whole printing process took approximately 5 h.

Wherever possible, the printed components were removed from the build plate by electro-discharge machining (EDM). Each dumbbell-like block was further laser-cut (sliced) to obtain sub-sized tensile specimens approximately 5 mm thick.

### 2.3. Microstructural characterisation

#### 2.3.1. Optical and scanning electron microscopy

The cp-Ti, BN, and Ti-BN powders were analysed using a scanning electron microscope, SEM (TM4000Plus, Hitachi) to observe the morphology of the respective particles and verify the mixing of cp-Ti particles and BN nanosheets after ball milling.

Printed cube-like samples were mounted in epoxy resin (Struers ProntoPress 20). A thin layer of material was then removed (Kemet cutting machine) in order to expose a fresh metal surface. Subsequently, the samples were ground smooth on silicon carbide papers (from 100 grit to 2000 grit, under continuous water flow) and then polished (Struers RotoPol-22) on a cloth imbued with an oxide polishing suspension (OPS) of colloidal silica particles with 2 vol% of ammonia and 2 vol% of hydrogen peroxide. The polished samples were washed with running water and pH-neutral detergent, and carefully cleaned with cotton wool. The samples were finally flushed with ethanol and dried using a compressed air gun. The polished surfaces were preliminarily imaged using an Olympus GX71 Optical Microscope (OM), with polarising filters operated under the High Dynamic Range (HDR) settings.

#### 2.3.2. Bulk X-ray diffraction

X-ray diffraction (XRD) was run under different conditions for the feedstock powders and the printed parts.

A Bruker D8 Advance A25 X-ray Diffractometer operating under CuKα radiation (40 kV, 40 mA) equipped with a Lynx Eye XE-T detector was employed to obtain the diffractograms of the individual cp-Ti and BN powders. The samples were scanned over the 2θ range 5°–130° with a step size of 0.02° and a count time of 1.6 s per step, and were spun at 15 RPM during data collection.

A Rigaku SmartLab, equipped with a rotating anode CuKα source (45 kV, 200 mA), and Hypix 3000 detector, was employed to test the as-printed cubes. The diffractometer was operated in Bragg-Brentano mode with a 1° incidence slit, 20 mm receiving slit and a beam limiting mask of 5 mm. Data was collected over the 2θ range 5°–130° with a step size of 0.01° and a scan rate of 2° per minute.

The collected XRD data was analysed using the Bruker XRD search match program EVA 6, and crystalline phases were identified against the ICDD-JCPDS powder diffraction database. The average crystallite size and strain were preliminarily estimated through the Williamson-Hall plots [14]. Details about the method are provided in the Supporting

Information, Section SI.1.

For higher accuracy, a Rietveld analysis (Bruker TOPAS V6) was also completed to determine the lattice parameters, anisotropic ("a" and "c" direction) crystallite size, strain, and additional preferred orientation along the (0 0 1) direction. Background signal was described through a combination of Chebyshev polynomial linear interpolation function and 1/x function. Cell parameters, vertical sample displacement, peak full width at half maximum, and scale factor were all refined. Anisotropic crystallite size and preferential orientation were calculated in TOPAS using custom functions based on the contributions by Ectors et al. [15] and by Zolotoyabko [16], respectively. Error ranges were calculated based on three estimated standard deviations as determined by TOPAS.

#### 2.3.3. Electron back-scattered diffraction

The electron back-scattered diffraction (EBSD) measurements were conducted on a JEOL-FEG Scanning Electron Microscope operating at an applied voltage of 20 kV. The electron beam was rastered across the sample (tilted by 70° about the horizontal plane) with the orientation Kikuchi patterns captured using an Oxford EBSD detector. Aztec Crystal software [17] was used to plot the inverse pole figure orientation maps and the reconstructed prior-β orientation maps.

#### 2.3.4. Small- and wide-angle X-ray scattering

Small-angle X-ray scattering (SAXS) and wide-angle X-ray scattering (WAXS) measurements were performed on a Xenocs-Xeuss3.0 SAXS-WAXS system at the InSitX X-ray facility [18]. The SAXS-WAXS instrument is based on a Ga–In liquid metal jet X-ray source, with monochromatic X-rays based on the GaKα characteristic (1.3476 A). The source was operated at 70kVP and 250W. Based on a transmission experiment, the scattering signal was acquired using a Pilatus 1 M area detector and the X-ray spot size set to 0.8 mm × 0.5 mm for the SAXS measurements and to 1.6 mm × 0.9 mm for the WAXS measurement. The sample-to-detector distances for the SAXS and WAXS measurements were 1800 and 60 mm, while the data collection time was 180 s and 1800 s, respectively. The scattering images were processed using XSACT software [19].

#### 2.3.5. Micro-computed tomography

Micro-computed tomography (micro-CT) measurements were performed to inspect the build quality in small printed components (rods). Polychromatic X-rays from a tungsten X-ray source operating at an applied voltage of 90 kV and 25 μA were employed. X-ray projection data was recorded using a Photonic-Science detector. During tomography measurement, the sample was rotated about 360° in steps of 0.5° with an image acquisition time of 15 s/step. Image reconstruction and visualisation was carried out using X-TRACT [20] and AVIZO [21] software packages, respectively.

### 2.4. Mechanical characterisation

#### 2.4.1. Vickers microhardness

Vickers microhardness (Buehler Micromet 2013 Microhardness Tester) was measured on freshly polished surfaces (prepared as per OM imaging, above) under an applied load of 100 $g_f$ and 300 $g_f$. Average value and standard deviation were calculated on 10 indentations.

#### 2.4.2. Tensile tests

As previously mentioned, sub-sized tensile specimens (nominal gauge length of 21 mm and cross section of 5 mm × 5 mm; filler radius of 4 mm) were laser-cut from the dumbbell-like blocks, which led to obtaining 4 samples for cp-Ti and 3 samples for Ti-BN, as the fourth Ti-BN specimen broke while being laser-cut. Uniaxial tensile tests were conducted on an Instron 4505 universal testing machine equipped with a 100 kN load cell. For comparative purposes, the same strain rate of 0.02 mm/s was applied to all specimens. The Young's modulus (E), the ultimate tensile strength (UTS), and the elongation at break (EAB) were estimated through data analysis of the (engineering) stress-strain curves.

### 2.5. Anisotropy

To account for the predictable anisotropy of AM parts [4,22,23], all analyses on the cube-like samples (including OM, XRD, and HV measurement) were repeated on the top and side surfaces of the as-printed components, where "top" surface refers the part's face normal to the growth direction (i.e., parallel to the build plate), whilst "side" surface refers to any of the part's faces parallel to the growth direction (i.e., normal to the build plate). With the raster angle being changed on each printing layer, it was assumed that all "side" faces parallel to the growth direction ("z" axis) were equivalent, irrespective of their relative orientation to the "x" and "y" (in-plane) axes.

## 3. Results

### 3.1. Powder pre-mixing

The Ti-BN feedstock is shown in Fig. 1. The long-time, low-energy pre-mixing favoured the even distribution of BN nanosheets on the surface of the larger Ti particles, which retained their original spherical shape and size.

### 3.2. Print quality

As demonstrated in Fig. 2, 3D parts could be built successfully with the Ti-BN powders, and all geometries were neatly produced with flat surfaces and sharp edges. However, macroscale cracks originated from the sides of the Ti-BN samples and propagated inwards normal to the build direction. Fractures were more obvious in larger parts (i.e., dumbbell-like blocks for tensile tests) than in smaller ones (i.e., cubes and cylinders), whilst rods were perfectly sound.

Under the OM, both the cp-Ti parts and the BN-modified ones appeared fully dense, without any detectable microporosity (Supporting information, Figure SI.1). However, it was not possible to distinguish any features relating to the α-Ti grain texture, in spite of working under polarised light.

While the OM inspection of the cross section of the Ti and Ti-BN cubes did not reveal major microstructural defects, an X-ray micro-CT investigation was conducted on the rods in order to verify the growth and preferential distribution of pores along the build direction in slender geometries (Supporting information, Figure SI.2). After scanning each rod, a threshold image was created to separate the region of interest (i.e., pores) from the matrix. The volume and the mean ferret diameter were then evaluated from the segmented pores. Very few micro-pores could be detected in both materials, and they were preferentially located in the upper part of the rods, which was particularly evident for Ti-BN.

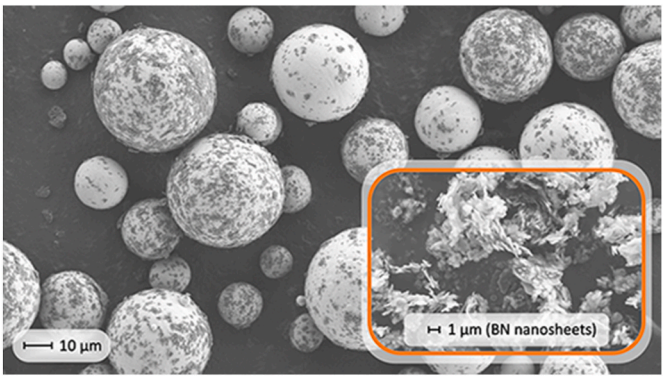


**Fig. 1.** Cp-Ti particles coated by BN nanosheets (shown in the inset) after pre-mixing. Scale bar: 10 μm for main figure; 1 μm for inset.

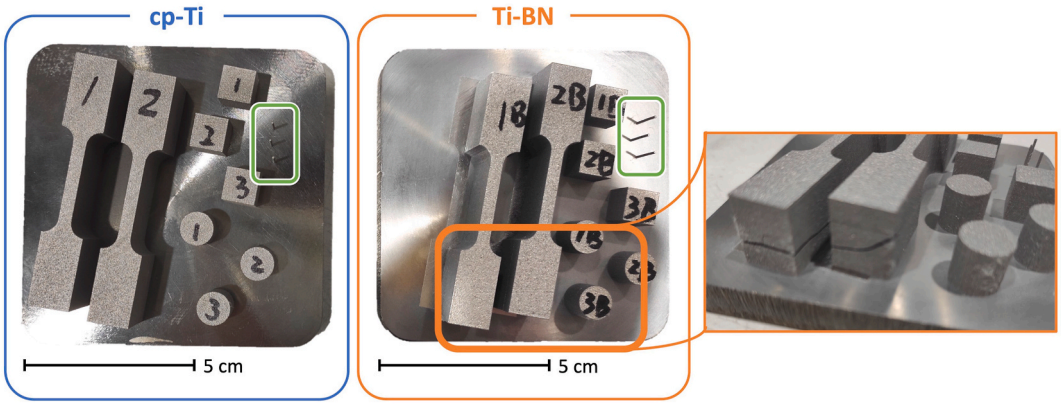


**Fig. 2.** Cp-Ti (left) and Ti-BN (right) parts before being separated from the build platform by EDM. Some Ti-BN parts were cracked, as shown in the detail. Green rectangles help visualise the as-printed rods.

Notably, the mean pore diameter was slightly lower for Ti-BN (13 μm) than for cp-Ti (19 μm).

### 3.3. Microstructure

#### 3.3.1. Phase composition and texture through bulk XRD

After testing the cp-Ti and BN feedstock powders as a term of comparison (Supporting information, Figures SI.3 and SI.4), XRD was used to study the phase composition of the printed samples (Supporting information, Figures SI.5 and SI.6; for clarity, all diffractograms are shown in the 30°–80° 2θ range). All peaks in the diffractograms of the cp-Ti and Ti-BN cubes could be attributed to the α-Ti phase. This corroborates the complete transformation from (body-centred cubic, BCC) β-Ti to (hexagonal close packed, HCP) α-Ti upon cooling. Meanwhile, it was not possible to detect the presence of any intermetallics, either borides or nitrates, being generated by the reaction between Ti and BN. Similarly, the diffractograms did not present any peaks attributable to unreacted BN.

The results of the Williamson-Hall analysis listed in Table 1 should be considered with care, due to the strong scattering (tables and diagrams with raw data are provided in the Supporting information, Section SI.6). The R-squared value ($R^2$), which correlates with the linearity of the Williamson-Hall plots, was on average higher for the Ti-BN samples than for the cp-Ti counterparts, which suggests a less textured grain structure. However, unlike the cp-Ti parts, the Ti-BN samples appeared to be strongly strained, which could be attributed to the unoptimized printing parameters. As for the average crystallite size, the results of the Williamson-Hall analysis were inconclusive.

The outcome of the Rietveld analysis is summarised in Table 2. The crystallite size was systematically higher in the "a" direction than in the "c" direction for both materials, due to the lamellar morphology of α-Ti grains, but it was remarkably refined by the addition of BN. The aspect ratio (calculated as the ratio between the crystallite size in the "a" direction and the crystallite size in the "c" direction) was comparable on the top surface, but dramatically reduced on the side surface after adding BN. The strain was negligible on the top surface of both materials' cubes. However, thermal stresses built up along the growth direction, which led to strain being present on the side surfaces. According to the Rietveld analysis, the strain was much stronger in the Ti-BN cubes than in the cp-Ti ones, which was consistent with the estimates of the Williamson-Hall model. While there was still some preferred orientation along the (0 0 1) direction in the Ti-BN cubes, it was notably lower than in the cp-Ti cubes.

**Table 1**
Results of the Williamson-Hall analysis conducted on the top and side surfaces of the cp-Ti and Ti-BN cubes, including the R-squared value ($R^2$) of the linear fit.

| Parameter | cp-Ti, top | cp-Ti, side | Ti-BN, top | Ti-BN, side |
|---|---|---|---|---|
| Strain, ε | 0.0009 | 0.0016 | 0.0029 | 0.0027 |
| Crystallite size, L [nm] | 34.5 | 50.0 | 53.7 | 34.5 |
| $R^2$ | 0.3188 | 0.4675 | 0.614 | 0.5088 |

**Table 2**
– Outcome of the Rietveld refinement conducted on the top and side surfaces on the cp-Ti and Ti-BN cubes.

| Parameter | cp-Ti, top | cp-Ti, side | Ti-BN, top | Ti-BN, side |
|---|---|---|---|---|
| *a* parameter [Å] | 2.9564 (2) | 2.9561 (2) | 2.9566 (2) | 2.9561 (2) |
| *c* parameter [Å] | 4.6861 (2) | 4.6861 (3) | 4.6913 (4) | 4.6899 (4) |
| Crystallite size, *a* direction [nm] | 28(4) | 28(3) | 20(1) | 22(2) |
| Crystallite size, *c* direction [nm] | 18(2) | 13(1) | 13(1) | 14(2) |
| Aspect ratio ("*a*" size/"*c*" size) | 1.56 | 2.15 | 1.54 | 1.57 |
| Strain, ε [%] | 0 | 0.026 (9) | 0 | 0.139(6) |
| Additional preferred orientation in the (0 0 1) direction [%] | 25.4(2) | 20.7(2) | 18.0(2) | 14.8(2) |

#### 3.3.2. Grain morphology, orientation, and micro-texture through ESBD

EBSD was used to study the grain morphology, orientation and micro-texture changes in cp-Ti and Ti-BN builds in more detail (Fig. 3).

The microstructure for all samples was successfully indexed with α-Ti, while the presence of residual β-Ti was almost negligible, in agreement with the bulk XRD. For all maps the colouring was used to represent the orientations plotted according to inverse pole figure with respect to the build direction. Owing to the grain size, high and low resolution EBSD maps were necessary. For cp-Ti (Fig. 3a), the microstructure map highlights the elongation of α grains, consistent with the epitaxial growth commonly observed in AM [10]. In general, the microstructure consisted of coarse α lath structures with large α grains. Smaller dark patches were also observed in the map, which were due to unresolved small α grains typically less than 3 μm in size. In the initial data acquisition process, the first grain orientation map recorded for the Ti-BN sample at the same step increment of 0.5 μm resulted in many failed indexation results with no reliable data. Consequently, a slightly smaller map with a finer step size of 0.04 μm was employed, and the results are displayed in Fig. 3b. The Ti-BN microstructure exhibited a combination of Widmanstäten and basket-weave α grain morphology.

The identified grains from the channel 5 software package were then segmented using AVIZO software to determine the length and width of the α laths (Supporting information, Figure SI.11). The average length and width of the α laths in cp-Ti were 3.1 and 1.1 μm, respectively, while the larger α grains were about 20 μm wide and extended to over 100 μm. On the other hand, the laths in the Ti-BN builds were homogeneous, with

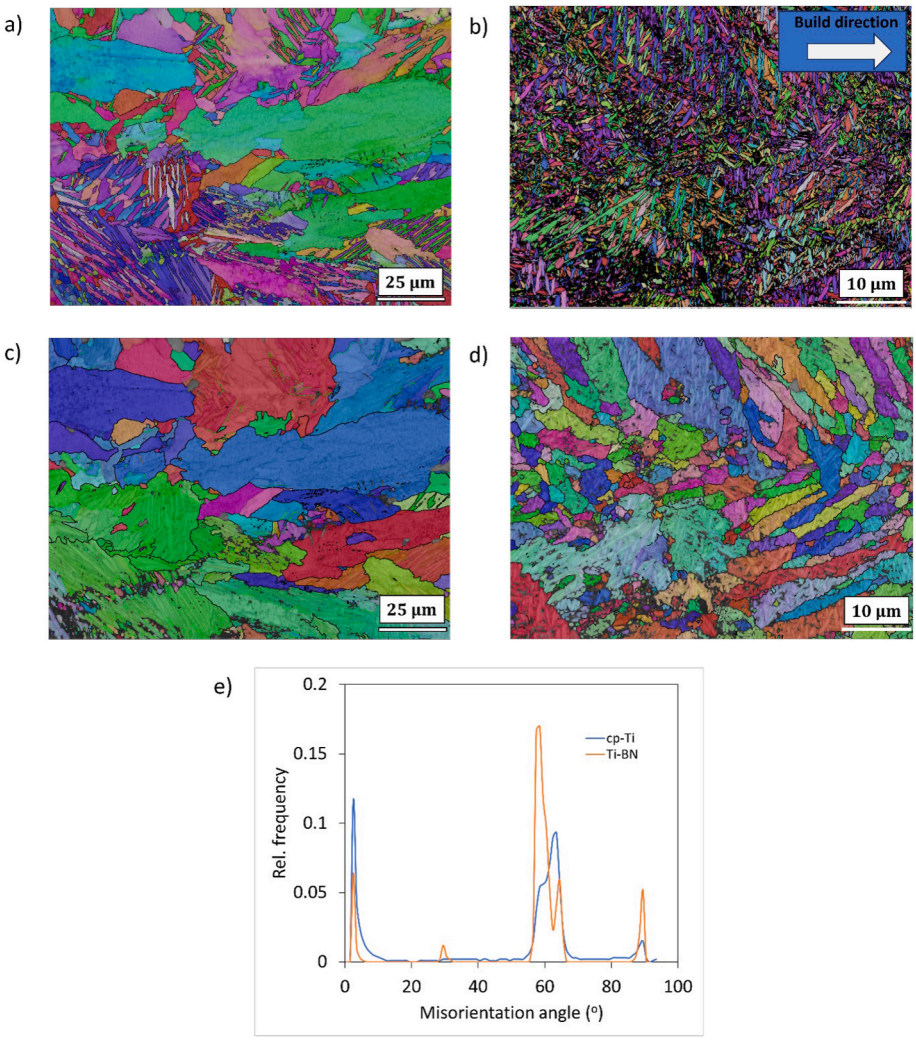


**Fig. 3.** – EBSD results: orientation maps of the α-Ti phase in cp-Ti (a) and Ti-BN (b) samples; corresponding reconstruction of prior β grains in cp-Ti (c) and Ti-BN (d) samples; misorientation angle distribution (e).

the length and width being reduced significantly to 0.46 and 0.15 µm, respectively.

The estimation of prior β grain size provides additional information regarding the change in grain size triggered by the addition of BN. Prior β grains were reconstructed using the Burgers orientation relationships between the α and β phases ({0001}α//{101}β and <11–20>α//<111>β) for the β-to-α transformation in the AZtecCrystal software. The reconstructed images of the parent β grains are shown in Fig. 3c and d for cp-Ti and Ti-BN, respectively. Clearly, the cp-Ti microstructure was templated on larger prior β grains compared to the Ti-BN counterpart. Prior β grains were elongated along the build direction in both materials due to epitaxial growth promoted by the layer-by-layer build process. However, the average prior β grain size decreased from 19 ± 13 µm for cp-Ti to 5 ± 3 µm for Ti-BN, which corresponds to a decrease in size of nearly 4 times. There did not appear to be any real preferential decrease in the measured grain aspect ratio, whereby the length was estimated to be reduced by about 4.2 times, and the width by about 5 times.

Owing to the limited grain statistics for the fine step size EBSD maps, orientation data for the low resolution maps was employed. The EBSD data highlighted a slight texture change between the two samples. Quantitative analysis of the orientation data indicated an increase above the random texture of 1.9 for cp-Ti and of 1.4 for the Ti-BN alloy. These results acquired at the microscale corroborate the bulk XRD data, where a more random orientation was identified for the Ti-BN sample, while also providing additional detail about the α and prior β size and morphology.

Fig. 3e shows the misorientation angle distribution plots of α laths in cp-Ti and Ti-BN builds. The identification of three peaks at around 60° and a single peak at 90° is attributed to the formation of α variants determined by Burgers orientation relationships as the β phase transforms to α upon cooling. It is clear from the plots in Fig. 3e that certain α variants at 60° and 90° are promoted in the presence of BN, which is consistent with similar observations in the literature [9].

From the high-resolution EDS maps collected with the EBSD analysis (Supporting information, Figure SI.12), regions with B and N enrichment with a simultaneous depletion in Ti can occasionally be seen. This suggests the presence of a small amount of residual BN particles in the Ti-BN samples. Meanwhile, no additional phases such as TiB or elemental B could be identified.

### 3.3.3. *Morphological investigation through SAXS-WAXS*

For the SAXS-WAXS measurements, X-rays were incident on the samples perpendicular to the build direction. The WAXS results are shown in Fig. 4a and b for cp-Ti and for Ti-BN, respectively. Three rings corresponding to the [10–10], (0002) and [10,11] reflections were seen for both materials. However, a clear difference could be observed in the scattering, in that the rings for cp-Ti were discontinuous, thus indicating the presence of large grains or preferred orientation in the microstructure, while the rings for Ti-BN displayed a randomized texture in the α grains, in good agreement with the EBSD results. No additional rings

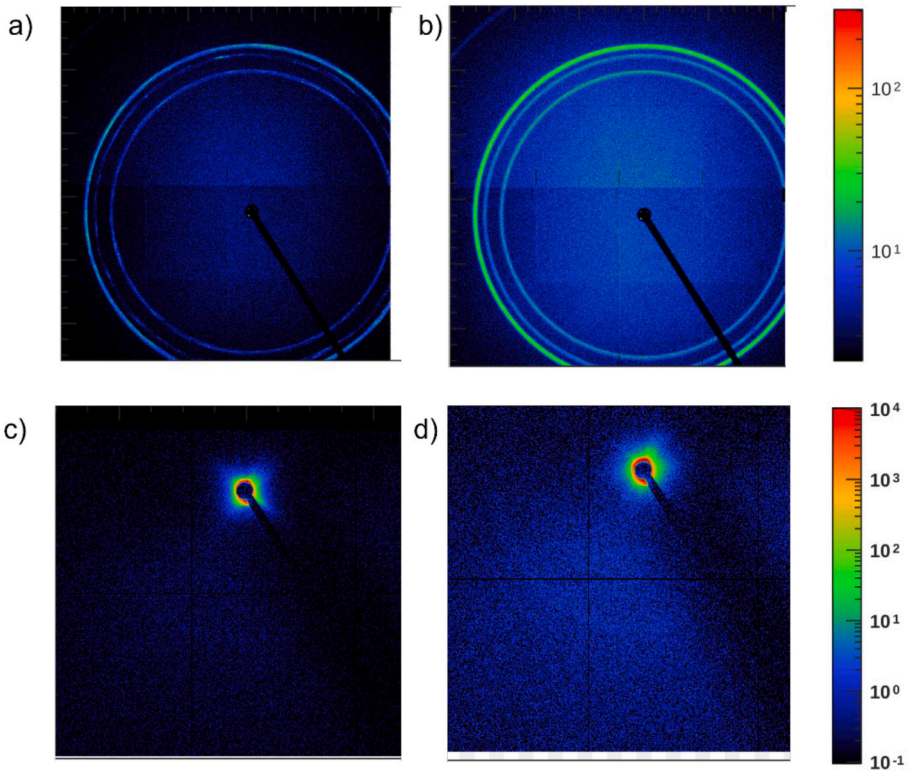


**Fig. 4.** – WAXS (a, b) and SAXS (c, d) results collected on the same area of the sample for cp-Ti (a,c) and Ti-BN (b,d).

corresponding to the β phase could be detected.

The SAXS analysis, on the other hand, provided additional information regarding the morphological changes in the microstructure associated with the addition of BN. The results of SAXS for cp-Ti and for Ti-BN are shown in Fig. 4c and d, respectively. It is to note that the SAXS signal was primarily focussed close to the beam stop. This indicated the presence of relatively coarse structures (in the micrometre range) in both cp-Ti and Ti-BN builds. Further, the scattering from the cp-Ti sample exhibited a 4-fold symmetry (Fig. 4c), thus depicting two distinctively oriented α lath morphologies in approximately 45° angle to the build direction. Conversely, in the case of Ti-BN the scattering appeared to be closely circular (Fig. 4d), with randomly distributed spikes on the scattered data indicating nearly randomized orientation of α laths mostly governed by the refined grains in the presence of BN.

### 3.4. Mechanical properties

Consistent with the results reported in the literature [10], the addition of Ti-BN nearly doubled the Vickers hardness of the base cp-Ti irrespective of the surface being tested (be it either top or side), as demonstrated by the bar charts in Fig. 5. Notably, the effect of the applied load was negligible for both cp-Ti and Ti-BN, likely due to their dense microstructure.

The engineering stress-strain diagrams acquired under tensile loading are plotted in Fig. 6. The results of the tensile tests (average values based on 4 samples) show that, thanks to the optimised printing parameters, the cp-Ti parts featured high strength (UTS = 519.8 ± 9.9 MPa) and stiffness (E = 105.9 ± 7.2 GPa), coupled with excellent ductility (EAB = 26.8 ± 5.9%). Due to the as-printed parts being cracked, only three dumbbell-like specimens could be laser-cut from the Ti-BN blocks. Out of them, two specimens failed prematurely, and did not achieve a steady linear elastic deformation regime before breaking (inset in Fig. 6b). The behaviour of these two specimens was reasonably dictated by cracks being present even before testing, although not visible to the naked eye. Ultimately, only one Ti-BN dumbbell-like specimen could be tested successfully, which impedes the assessment of any statistically meaningful result. Tentatively, it may be suggested that the addition of BN increased the stiffness (with the only measured value of E

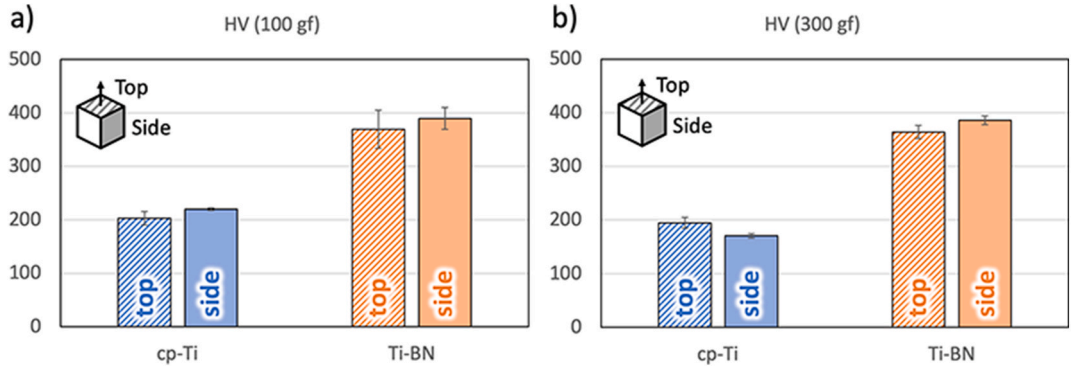


**Fig. 5.** Vickers hardness (HV) measured on the top and side surfaces of the cp-Ti and Ti-BN cubes under different applied loads of 100 $g_f$ (a) and 300 $g_f$ (b).

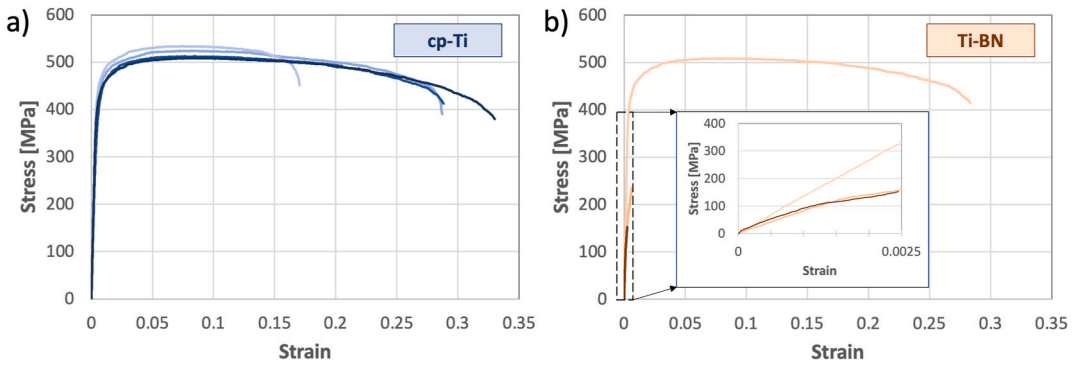


**Fig. 6.** Engineering stress-strain curves acquired under tensile loading for cp-Ti (a) and Ti-BN (b) dumbbell-like specimens.

being 133.2 GPa), while leaving the strength unchanged (UTS = 508.7 MPa). Interestingly, the EAB was as high as 28.3%. It is important to reiterate that these values should be considered with caution as they refer to only one specimen. However, there are signs that, if printed under proper parameters, Ti-BN may be as ductile and strong as cp-Ti, while offering increased stiffness.

## 4. Discussion

### 4.1. BN-driven microstructural changes in Ti-based AM components

In metal AM, many processing variables can be manipulated to favour the achievement of refined and equiaxed grains. For example, the grain morphology, grain size, and texture are governed by the local thermal conditions during solidification, whereas the transformed microstructure is dictated by the post-solidification cooling rate. In practice, the laser power, laser spot size/shape, and laser traverse speed play an important role in controlling the thermal history and, hence, in driving the final microstructure [24]. However, equiaxed microstructures are still difficult to achieve without the addition of nucleant particles [5].

High-intensity ultrasound applied during the crystallisation process from liquid to solid has the potential to change the microstructure of the resulting crystalline material, and ultrasonic grain refinement has been successfully demonstrated for Ti–6Al–4V [5]. This approach does not imply any modification to the chemistry and "cleanliness" of the metal powder. However, it does require a dedicated printing set-up in order to combine AM and ultrasonic vibration.

Post-printing heat treatments can be applied to modify the distribution, size, and morphology of the α phase, but they typically have a limited effect on the prior-β grains [24].

Finally, the addition of boron appears to be a convenient strategy to induce grain refinement and mitigate columnar grain growth, because it effectively acts on both the prior-β grains and the α laths without any specialised printing hardware [10]. Notably, the action of boron is so strong that even trace amounts are sufficient to modify the microstructure of Ti and its alloys. This is fundamental to reduce the risk of agglomeration of the additive in the melt pool, and also to meet stringent specifications on the printed parts' chemistry, such as the prescriptions of ASTM F2924-14(2021) [25] for Ti–6Al–4V parts produced by PBF.

BN is commonly used in AM as a source of B for controlling the microstructure and, hence, the properties of Ti-based parts. In particular, nanosized BN has been receiving much attention owing to the enormous specific surface area available for interacting with the laser beam (or electron beam, or plasma, depending on the AM technology) and with the surrounding metal matrix [9,26,27].

According to thermodynamic considerations, in the temperature range between 500 K and 2000 K the most likely reactions between Ti and BN lead to the formation of either TiB or $TiB_2$ and TiN [28,29]. In principle, the formation of $TiB_2$ should be thermodynamically favoured over the formation of TiB. However, TiB is predominant, because the growth rate of $TiB_2$ crystals is much slower than that of TiB [30]. Moreover, $TiB_2$ is known to react with Ti leading to the formation of additional TiB if the concentration of B in the reaction zone is below 18–18.5% [28,31,32].

While the complete consumption of BN and the subsequent formation of TiB and TiN are predicted to occur under equilibrium, the high energy density delivered by the laser beam and the fast cooling rates typical of PBF-LB may promote out-of-equilibrium reactions [33]. Partly unreacted BN particles may survive into the printed part [9,26–28]. Meanwhile, laser processing may cause a selective depletion in N [9,27,34]. The remaining N rapidly diffuses away from the original BN particles. For relatively low concentrations (below 8 wt%), N is likely to become an interstitial at high temperature, and then to remain entrapped as super-saturated solute in the matrix as a result of fast cooling [27]. At higher concentrations, various Ti nitrides can also form [28,35,36].

As for the presence of B, the Ti–B system presents a binary eutectic corresponding to a composition of Ti-1.6B (wt.%) at a temperature of 1540 °C [37]. However, the melt pool in AM is a highly dynamic environment, and the local concentration of B may not correspond to the nominal one [38]. Moreover, fast cooling as commonly observed in most AM methods may cause the entrapment of B in a super-saturated matrix, thus leading to a shift of the eutectic point [39].

Upon cooling, for (locally) hyper-eutectic concentrations, primary TiB will solidify first from the melt, typically in the form of elongated prismatic crystals. When the system reaches the eutectic temperature, Ti solidifies in its β form partly through heterogeneous nucleation at primary TiB crystals, partly through homogeneous nucleation from the melt. Since the solubility of B in solid Ti is nearly null, B atoms are progressively rejected from the newly formed β-Ti crystals to the surrounding liquid, where they react with the residual molten Ti and precipitates in the form of eutectic TiB nanowhiskers. It has often been observed that eutectic TiB nanowhiskers, as well as primary TiB precipitates, are forced to the β-Ti grain boundaries, where they arrange themselves in a quasi-continuous network, which survives to room temperature through the β-to-α ("β-transus") transformation occurring at 882 °C [11,12,40,41]. As previously mentioned, due to fast cooling in PBF-LB, B atoms may sometimes be locked-in as super-saturated solute in the Ti matrix. Re-heating due to the deposition of subsequent layers may initiate the eutectic reaction between super-saturated B and Ti, which leads to the growth of intra-grain TiB crystals [34,42,43].

For (locally) hypo-eutectic systems, the first solid that crystallises upon cooling is β-Ti, while TiB will only form through the eutectic reaction in the liquid pockets surviving between primary β-Ti grains [44]. Upon cooling, the Ti matrix undergoes the β-to-α transition, leading to a composite system where TiB is still prevalently located at the grain boundaries.

In AM processes, B exerts a strong grain refining effect on β-Ti due to

the nucleant and solute effects mentioned above. Since the growth of α-Ti grains at the β transus is largely templated by pre-existing β-Ti grain boundaries, the reduced size of prior β-Ti grains promotes the formation of refined and more isotropic α laths, reduces the α colony size, and often suppresses grain boundary α [45]. Moreover, a weakened texture is generally observed, due to the reduced epitaxial (columnar) growth of β-Ti grains [46], and due to the possible nucleation of α grains on TiB precipitates instead of prior β-Ti grain boundaries [47]. The refined and randomised microstructure can then be retained in spite of re-heating during the deposition of subsequent layers thanks to the pinning effect of TiB crystals at the grain boundaries [48,49].

### 4.2. Print quality

Due to the altered thermo-physical properties associated with the presence of a second phase, metal matrix composites (MMCs) generally require different printing parameters than the base metal for achieving high-quality defect-free parts. Most ceramic phases, BN included, have a higher laser absorption coefficient than Ti [50]. Moreover, thermodynamically favoured reactions between the filler and the matrix are exothermic, which provides an additional energy input to the melt pool in the form of heat. Finally, ceramic nanoparticles are likely to adhere to the surface of the larger metal powder, and this increases the surface roughness and hence reduces the laser reflection [50,51]. Ceramic particles may also contribute to bridging adjacent metal particles, thus favouring consolidation [27]. As a result, in theory, adding a ceramic phase would be expected to make printing easier. However, it is common experience that ceramic-metal powder mixtures actually require a higher energy density than neat metals or alloys for printing. This is mainly because most ceramic phases are thermally stable and melt at a much higher temperature than the base metal [52]. The presence of solid (unmolten) particles disrupts the melt pool dynamics, and this has profound consequences on the melt pool geometry and ultimately on the consolidation of the printed part [53].

Although it was predicted that this would result in print defects, in the present contribution it was decided to process the Ti-BN powders with the same printing parameters routinely used for cp-Ti. This was for several reasons. Firstly, because this scenario most likely corresponds to what happens in industry, where most printers are “black boxes” pre-programmed with proprietary “parameter sets” that the printer’s manufacturer has optimised for common metals and alloys [54]. Oftentimes, the choice is limited to a handful of metals and alloys, such as tool and stainless steels, Ti and Ti–6Al–4V, Ni–Ti (nickel-titanium) alloys, and copper. As a result, if faced with a new feedstock like the pre-mixed Ti-BN powders being considered here, the operator would likely have to select the printing parameters among those few options that are already available in the printer’s menu, and, in that case, cp-Ti could certainly be an educated guess. Secondly, in terms of scientific research, printing both materials under the same conditions was deemed necessary to single out the effect of adding BN. On the other hand, observing the outcome of the printing parameters optimised for Ti when applied to Ti-BN represents the most logical starting point for the optimisation of the printing parameters of the new material. In this regard, it should also be mentioned that the contributions by Otte et al. [26,27] provide a detailed optimisation of the printing parameters of Ti-BN systems with compositions that closely correspond to the one being examined here. However, despite offering a useful term of comparison, these parameters were identified for a specific printer, and therefore they could not be directly translated to a different equipment, as it is well known that manufacturing the same material on different printers requires different parameters [55].

In conclusion, the presence of cracks in the Ti-BN parts, as shown in Fig. 2, was not unexpected. Despite the advantages offered by the addition of B towards the microstructural design of Ti-based AM parts, the difficulty of defining appropriate processing parameters and the impossibility of translating them onto most printers working as “black boxes” may represent a substantial obstacle to the wider uptake of B-modified feedstocks in industry.

In spite of the presence of macroscale cracks (Fig. 2), the microstructure of the Ti-BN parts was extremely homogeneous and compact, without any visible porosity, as evidenced by the OM images (Supporting information, Figure SI.1). Micro-pores could be occasionally observed through micro-CT scanning (Supporting information, Figure SI.2), but defects are inevitable in AM parts [56], and the formation of pores may be exacerbated in very thin parts built normal to the base platform like the rods used for the micro-CT tests [57,58]. Achieving nearly pore-free parts was certainly favoured by the low-energy procedure followed here for mixing Ti and BN, since ball milling did not alter the original spherical shape and size distribution of the cp-Ti powder specifically designed for PBF-LB.

### 4.3. Microstructure: preliminary characterisation through bulk XRD

The phase identification through bulk XRD (Supporting information, Figures SI.5 and SI.6) confirmed the complete conversion of the high-temperature β-Ti polymorph to the low-temperature α-Ti polymorph, as expected in systems that do not contain β stabilisers [59].

Sometimes, the presence of α′ martensite is also reported in the literature [60]. However, the formation of α′ martensite is largely dependent on the processing conditions [61] and the nature of the feedstock powder [62]. As a result, depending on the printing parameters and the system composition, it is not uncommon to observe α-Ti, rather than α′ martensite, in Ti parts processed by PBF-LB [63]. Moreover, the addition of B may favour the crystallisation of α forms at the expense of α’ martensite [28,49,64].

Not surprisingly, bulk XRD could not reveal any trace of intermetallics (TiB included) being generated by the reaction between BN and Ti, nor the presence of any residual unreacted BN, because the respective weight fractions were too low for detection. This is a known issue with Ti–B systems modified with trace amounts of B [9,39,47,49,51,65,66]. Besides the low concentration, confirming the presence of TiB is particularly challenging due to the overlap of most TiB and α-Ti peaks [46].

Although the Williamson-Hall method was originally proposed for powdered samples [67], the analysis conducted on the printed components reveal two interesting trends. Firstly, the strain in the Ti-BN parts is, on average, much higher than in the cp-Ti counterparts. Micro-strain is due to residual stresses being built-in upon printing [68]. As mentioned above, the Ti-BN parts were processed under unoptimized parameters, which may have worsened the residual stress state with respect to the cp-Ti parts [69]. Concurrently, the addition of B is known to decrease the ductility of Ti [9,40,70], and this phenomenon may be exacerbated by the presence of interstitials, especially N [32]. The development of residual stresses, combined with the embrittlement of the Ti matrix (further confirmed by the results of the tensile tests), are likely the main physical reasons for the macroscale cracks observed in the Ti-BN parts, as discussed above (Section 4.2). Secondly, if the material was perfectly isotropic, all the points in the Williamson-Hall plot would lie on the same line [71]. Since scattering is observed in all plots for cp-Ti and Ti-BN (Supporting information, Section SI.6), the Williamson-Hall analysis confirms the anisotropic behaviour of the as-printed materials. However, the stronger data scattering suggests a higher degree of anisotropy in the cp-Ti parts than in the Ti-BN ones. The results of the Rietveld analysis (Table 2) are in good agreement with these trends, and also suggest that α laths are less elongated (lower aspect ratio) in the Ti-BN parts than they are in the cp-Ti cubes, which demonstrates the efficacy of B in promoting a less textured microstructure.

### 4.4. Structural features through advanced characterisation

The EBSD microstructures (Fig. 3) confirmed the development of α

lath morphology in both cp-Ti and Ti-BN samples. However, the addition of BN led to a significant refinement in the prior β grain size, which carried over to a significant refinement in α grains at room temperature. As discussed above, the reduction in the β grain size could be primarily associated with the increased nucleation sites available at the TiB crystals or near BN inclusions. Due to the very low concentration of BN used in the current Ti-BN system, the formation of TiB crystals could not be confirmed at the magnifications used for the EBSD microstructures. Even higher resolution and high magnification images would have been needed to this end. Nonetheless, the significant decrease observed in the prior β grain size is believed to be assisted by TiB, as often observed in Ti-based components produced by AM [10].

As already mentioned, the β-to-α phase transformation preferentially occurs through the formation of certain α variants, which tend to arrange themselves according to energetically favoured grain boundaries ("self-accommodation") [72–74]. As a term of comparison, Wang et al. [73] analysed the misorientation angle distribution of the α phase in cp-Ti sheets after solution treatment, water quenching and thermal annealing, and recorded the presence of four peaks located around 10° (frequency of nearly 0.01), 60° (nearly 0.18), 63° (nearly 0.15) and 90° (nearly 0.06). While the peak position matched closely, Fig. 3e shows that the relative frequency of the preferred misorientation angles for the cp-Ti samples examined here was slightly different, with the 63° angle prevailing on the 60° angle. However, the peak associated with the 60° misorientation angle became dominant again after the addition of Ti-BN. For both 3D printed materials, and especially for cp-Ti, the frequency of the 10° misorientation angle was significantly higher than it was for the samples investigated by Wang et al. [73]. These differences were likely caused by the competition between energy-driven self--accommodation and AM-induced epitaxial growth, with the preferential orientation of Ti grains in the AM samples being mitigated by the addition of BN.

Despite the decrease in size of the α laths in the Ti-BN samples, the aspect ratio appeared to be unchanged when compared to cp-Ti. Meanwhile, due to the substantial difference in morphology, a direct comparison of α lath texture evolution in cp-Ti with and without BN is not possible. The texture data from low magnification EBSD measurements present a more realistic picture of the orientation. A decrease in the texture strength from 1.91x random for cp-Ti to 1.43x random for Ti-BN indicates texture weakening due to grain refinement. The randomisation in the texture can also be seen from the continuous diffraction rings in the WAXS experiments. Further, a near spherical distribution in the SAXS signal indicates more available α lath orientations uniformly distributed in the fine prior β grains.

### 4.5. Mechanical properties

As shown in Fig. 5, adding BN in trace amount was enough to nearly double the Vickers hardness of the Ti-BN parts over the cp-Ti counterparts. This remarkable effect was predictable. Firstly, the addition of B generally increases the yield strength of the base metal, and this improves the material's resistance to plastic deformation and hence its hardness [12,28]. The strengthening effect of B is mainly driven by two mechanisms, i.e., Hall-Petch strengthening, and shear-lag strengthening [75]. The Hall-Patch strengthening effect, a.k.a. "boundary" strengthening, is associated with grain refinement, because the slip length of dislocations becomes shorter as the grain size is reduced [76]. The shear-lag strengthening effect, a.k.a. "load-sharing" or "load-bearing transformation", is associated with the presence of short fibre-like reinforcements, like the TiB crystals that are expected to form in B-modified Ti [77]. Reasonably, since the volume fraction of TiB in the Ti-BN parts being examined here is so low that it remains below the detectability threshold of XRD, it may be hypothesised that the main contribution to strengthening (and, thus, to hardening) will come from the Hall-Patch mechanism [78]. Nonetheless, as discussed by Li et al. [79], the overall strengthening effect is rather the result of the superposition of individual mechanisms, regardless of their specific entity. In addition to these strengthening mechanisms, the presence of TiB and other intermetallics may also impart additional hardness, since they are intrinsically harder than Ti [80]. Finally, another contribution to increasing the hardness of Ti comes from solute atoms, because N exerts a very strong solid solution hardening effect [9].

Ultimately, a remarkable increase in hardness is one of the main outcomes described in the literature when Ti-based AM parts are functionalised with BN. In order to support this statement, Fig. 7 maps the values reported in a number of published articles for the Vickers hardness of Ti- and Ti–6Al–4V-based parts processed by PBF-LB and by DED-LB as a function of the weight fraction of BN being added to the system. Further detail regarding each contribution analysed to draw Fig. 7 is tabulated in the Supporting information, Table SI.5.

In the absence of a standardised procedure for measuring the Vickers hardness of metal AM parts, different experimental conditions have been applied by different authors in the literature. For example, the indentation load spans two orders of magnitude, and the dwell time can also vary between 10 and 15 s. Since it is not possible to rule out the hypothesis that hardness values are affected by different indentation conditions [81,82], the comparison in Fig. 7 should be considered with caution. Nonetheless, it may be suggested that the hardness of Ti- and Ti–6Al–4V-based parts increases at first very quickly as the amount of BN increases, but then tapers off when the filler loading is 5 wt% or above, with the threshold lying indicatively in the 2–3 wt% range (dashed vertical lines in Fig. 7). The change in slope is still evident if the data regarding Ti-matrix parts manufactured by PBF-LB are plotted separately (shown in Fig. 7b). Naturally, additional data points would be required to further confirm these trends and, in case, to identify the critical filler loading in a more accurate fashion. However, this "saturation" in hardening can reasonably be associated with the "saturation" in grain refinement that is often observed when B is added to Ti and Ti alloys. In Ti and Ti alloy castings, the saturation limit for grain refinement is usually detected at around 0.10 wt% of B [74,83,84], but it has been postulated that the solute saturation point would shift to higher values in AM, especially in PBF-LB and DED-LB, due to the higher cooling rates [10]. For example, Zhang et al. [47] noticed that the size of the reconstructed β grains in Ti–6Al–4V parts processed by DED-LB kept decreasing up to 1 wt% of B. With the stoichiometry of BN being 1:1, given the atomic mass of B as 10,811 u and the atomic mass of N as 14, 0067 u, 1 wt% of B would correspond to 2.3 wt% of BN, which aligns well with the saturation limit in Fig. 7.

Besides this processing-induced shift of the saturation limit, other factors may also contribute to restraining the hardening effect at high filler loading. While a larger volume fraction of TiB and other hard intermetallics would likely form at higher BN loadings, these reaction products are expected to precipitate as coarse crystals, which are known to negatively affect the local ductility of the composite [70]. Moreover, at higher BN loadings there is a higher probability that unreacted/undissolved BN particles may survive into the printed part. While BN by itself is a hard material, the interface with the surrounding metal is likely to be very weak, as often observed for *ex-situ* composites [85]. The increasing concentration of thermally stable phases, which solidify at higher temperature than the metal matrix, is predicted to perturb the flow dynamics within the melt pool, thus favouring the development of pores and other microstructural defects [86]. Ultimately, these effects may impair the resistance to plastic deformation and hence the ductility of the composite. It should also be mentioned that, in terms of methodology, most models for calculating the indentation-induced area of contact are based on elastic equations, which generally assume that the elastic modulus of the material being tested remains constant with increasing depth of penetration [87]. As the concentration of BN, TiB and other reaction products increases, the composite becomes more heterogenous (which is also confirmed in the present contribution by the larger data scattering visible in Fig. 5 for the Ti-BN parts with respect to neat cp-Ti) and diverges from the theoretical models, which makes the

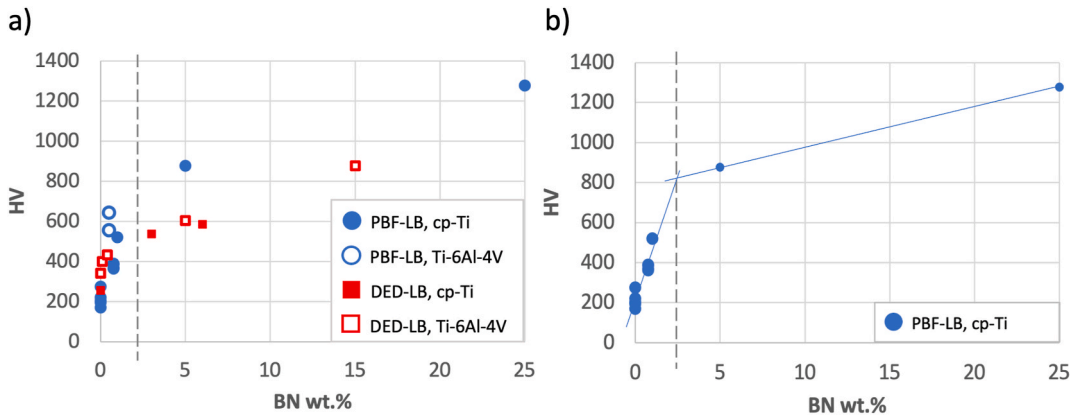


**Fig. 7.** – Comparison of literature data showing the effect of BN on the Vickers Hardness (HV) of Ti and Ti–6Al–4V parts processed by PBF-LB and DED-LB (a), with a focus on Ti parts manufactured by PBF-LB in analogy with the material being studied here (b). Dashed vertical lines in both (a) and (b) show the weight percent of BN indicatively corresponding to the saturation limit; faint blue lines in (b) show the linear trendlines for "HV" vs. "BN wt.%" corresponding to low and high concentrations of BN in Ti-based parts produced by PBF-LB.

interpretation of hardness data more uncertain.

The potential existence of a "hardening saturation effect" would deserve further attention in future, given the need of adding as little BN as possible while maximising the performance of Ti-based parts in order to preserve the printability of Ti.

The size of the indents produced on a relatively hard material like Ti is generally in the order of few microns. As such, although contact stresses may be transferred to the surrounding material while the tip is being pushed against the surface [88,89], Vickers hardness is still a "local" property, meaning that the tip probes a limited (sub-superficial) volume of material. Meanwhile, indents are preferentially located on defect-free areas of the material's surface. As a result, Vickers hardness is generally insensitive to the presence of cracks or other macro-defects, as it is quantified on an (arbitrarily chosen) "ideal" portion of material. Conversely, tensile tests return "global" properties, in that tensile loading is applied to the specimen as a whole, since the specimen is clamped in the grip sections and then tensile stresses are generated over the entire gauge volume (unless local instabilities occur [90]), where failure should occur for the test to be valid [91]. This explains why the drawbacks of adding BN under unoptimized printing parameters, namely the presence of residual stresses, the existence of macroscale cracks, and the embrittlement of the Ti matrix, could be better recognised through tensile testing, rather than through Vickers hardness measurement.

The results of the tensile tests conducted on additively manufactured parts can be affected by numerous variables. For example, in addition to materials composition and printing parameters, it is known that the tensile properties are influenced by the specimen size and shape, as well as by the testing conditions such as the loading rate. A recent assessment of applicable tensile test standards is available, for example, in the contribution by Crocker [92]. Given this complicated interplay, in the present research all the variables were kept the same while producing and testing the tensile specimens. This was purposely done in order to single out the effects of adding BN nanosheets to cp-Ti. As a result, the difference between the stress-strain diagrams in Fig. 6 is directly attributable to the presence of BN in the feedstock material. However, most of the Ti-BN specimens investigated here failed prematurely, which attests to the lack of structural reliability of the Ti-BN parts built under unoptimized parameters. The only dumbbell-like part that could be successfully laser-cut and tested returned very good tensile properties, but it is impossible to draw any sound conclusions from a single specimen. This reconfirms the paramount importance of printing the composite parts under optimised parameters to take full advantage of adding BN.

Unfortunately, the limited data available in the literature (for example, by Otte et al. ([27]) is not sufficient for mapping the tensile properties of Ti- and Ti–Al–4V-based AM parts against the weight fraction of BN as previously done for the Vickers hardness. Tensile testing is likely so uncommon in the body of literature because the lack of a dedicated standard for AM parts makes it difficult to conduct tensile tests in a systematic and repeatable way [55]. Moreover, it is often stated in the literature that compression tests are less sensitive to minor processing flaws than tensile tests are, and they also avoid necking instabilities [93]. As a result, compressive tests are frequently preferred to tensile tests in relation to metals processed by AM [12,75,94,95], especially for brittle materials [96] and parts without any post-treatment [34]. However, the limited understanding of the effect of BN on the tensile properties of Ti-based components processed by AM represents a serious gap, given the crucial role of tensile properties in materials selection and structural design. Moreover, tensile tests are important for recognising the impact of porosities and processing-related flaws on load-bearing capacity and reliability [97], particularly in fracture critical applications [55,98]. Accordingly, it is recommended that consideration be paid to tensile testing in future research.

Finally, the BN-modified parts presented in this contribution feature increased hardness, but also suffer increased brittleness with respect to their cp-Ti counterparts. The increased hardness, which is reasonably associated with a better resistance to plastic deformation [11,28], can be helpful in those applications that imply harsh contact conditions, mitigating wear and contact fatigue [99]. However, the increased brittleness may negate these advantages causing premature failure. As previously mentioned, the brittleness of the Ti-BN parts is to a large extent caused by the unoptimized printing conditions. However, the presence of boron per se is known to cause embrittlement. This issue has been often reported in the literature for both conventionally fabricated and additively manufactured parts [10]. It has been suggested that ductility can be partly restored by the addition of β stabilisers such as iron (Fe), molybdenum (Mo), and niobium (Nb) [32]. However, the co-existence of multiple additives deserves particular attention to figure out potential synergic or antagonistic effects. This approach would thus require additional research in future, especially in the AM panorama.

### 4.6. *Industrial scalability*

It is important to remark that the feedstock preparation presented here is extremely simple, cost effective and scalable. Naturally, the process needs some special attention in order to limit the oxidation of Ti and to safely handle the nano-sized BN nanosheets. Apart from that, at lab scale, the whole procedure can be easily accomplished with a glove

bag for pre-mixing cp-Ti and BN, and a roller to keep moving the plastic jars during the milling step. While scaling up is not foreseen to cause any major technological hurdle, the main criticality of this feedstock preparation method is the time required for milling, since the jars had to be left on the rollers and milled for 14 h at 50 rpm for the BN nanosheets to spread evenly on the Ti particles. However, provided that the spherical shape and size distribution of the Ti powder are preserved, it is reasonable to expect that this time could be cut down significantly with the adoption of industrial milling systems, instead of a (relatively rudimentary) roller. Moreover, the procedure described in the present contribution may appear particularly lengthy because it applies to the preparation of a single batch of feedstock powders, but the process could be made continuous to enable mass production.

Another important consideration is that, as previously remarked, the printing parameters pre-set for cp-Ti should be adjusted for Ti-BN. Although tuning the printing conditions falls outside the scope of this contribution, optimisation studies are common in the literature (for examples, in the papers by Otte et al. [26,27]) and could be similarly conducted for our material system. This would certainly facilitate the industrial uptake of the new pre-mixed powders presented, especially on those printers that work with "open" parameters, meaning that the operator can freely play with them. The adoption of the new Ti-BN powders remains more troublesome for those "black box" printers that only work with pre-set printing instructions. However, in broader terms, it is worth noting that this is an issue with all new feedstock materials, and not just with our pre-mixed powders, thus representing a potential obstacle to the translation of promising research outcomes in the literature to industrial practice.

AM is becoming mainstream in industry for the production of relatively small numbers of high-value components. While the productivity is still lower than conventional methods such as casting, metal AM enables the fabrication of complicated architectures and personalised constructs for performance-critical applications in the medical, energy, and aerospace sectors [100]. Further to this, being AM a tool-less technology, the targeted geometry can be changed effortlessly. However, it is generally recognised that the limited availability of printable materials is hindering the wider adoption of AM for broad-ranging functional customisation [101,102]. This ultimately leads to a paradoxical condition, whereby research is being geared towards the development of a broader range of printable materials, whilst most industrial printers are only designed to receive a limited number of basic materials. In future, overcoming this anomaly will likely require a closer connection between materials developers and technology suppliers.

## 5. Conclusions

Inroads into eliminating the epitaxial grain growth that causes columnar structures in additively manufactured titanium (Ti) parts have been demonstrated by the addition of low (0.77 wt%) amounts of boron nitride (BN) nanosheets. Monochromatic diffraction results from small- and wide-angle X-ray scattering (SAXS-WAXS) revealed that the addition of BN both refined the α-Ti grain size and randomized its texture. Coupling this with electron back-scattered diffraction (EBSD) data provides compelling evidence of the significant refinement of α-Ti grain. The grain refinement process is thought to be caused by the combined constitutional undercooling-solute effects enabled by boron (B), and by enhanced nucleation sites at BN or TiB during solidification of Ti melt, resulting in a B-enriched microstructure at grain boundaries. Further, the refined and randomised microstructure is retained in spite of reheating during the deposition of subsequent layers thanks to the pinning effect of TiB crystals at the grain boundaries. Optical microscopy supported by X-ray micro-computed tomography also revealed that the microstructure of the Ti-BN parts was extremely homogeneous and compact, largely due to the uniform adhesion of the BN nanosheets to the surface of the cp-Ti powder after low-energy ball milling. In terms of mechanical performance, the addition of trace amounts of BN almost doubled the Vickers hardness of the Ti-BN composite parts over the cp-Ti matrix. However, despite these observations in BN's ability to randomized the grain structure and improve the hardness of cp-Ti, the non-optimised printing parameters led to non-negligible residual stresses, Ti matrix embrittlement, and microscale cracks. These results herein suggest that the incorporation of BN into a Ti matrix for producing AM parts requires further investigation to optimize the 3D printing parameters, which may be an impediment to the wider uptake of BN-modified feedstock in industrial settings owing to the "black box" nature of most commercial printers.

## Declaration of competing interest

The authors declare that they have no known competing financial interests or personal relationships that could have appeared to influence the work reported in this paper.

## Acknowledgements

The team would like to thank the master students Yuanwei Wang for their help in preparing the CAD file for 3D printing, and Gayasha Godewatta Arachchige for their help with the micro-mechanical characterisation.

At the time of drafting this manuscript, AS and JJ were supported by CSIRO's Research Office through the Science Leader in Active Materials platform.

## Appendix A. Supplementary data

Supplementary data to this article can be found online at https://doi.org/10.1016/j.jmrt.2024.08.143.

## References

[1] Bermingham MJ, StJohn DH, Krynen J, Tedman-Jones S, Dargusch MS. Promoting the columnar to equiaxed transition and grain refinement of titanium alloys during additive manufacturing. Acta Mater 2019;168:261–74. https://doi.org/10.1016/j.actamat.2019.02.020.

[2] Attar H, Bermingham MJ, Ehtemam-Haghighi S, Dehghan-Manshadi A, Kent D, Dargusch MS. Evaluation of the mechanical and wear properties of titanium produced by three different additive manufacturing methods for biomedical application. Mater Sci Eng, A 2019;760:339–45. https://doi.org/10.1016/j.msea.2019.06.024.

[3] Jinschek J, Primig S, Proust G. Preface to the special issue: microstructure design in metal additive manufacturing—physical metallurgy revisited. J Mater Sci 2022;57:9525–6. https://doi.org/10.1007/s10853-022-07260-2.

[4] Carroll BE, Palmer TA, Beese AM. Anisotropic tensile behavior of Ti–6Al–4V components fabricated with directed energy deposition additive manufacturing. Acta Mater 2015;87:309–20. https://doi.org/10.1016/j.actamat.2014.12.054.

[5] Todaro CJ, Easton MA, Qiu D, Zhang D, Bermingham MJ, Lui EW, Brandt M, StJohn DH, Qian M. Grain structure control during metal 3D printing by high-intensity ultrasound. Nat Commun 2020;11:142. https://doi.org/10.1038/s41467-019-13874-z.

[6] Ralston KD, Birbilis N. Effect of grain size on corrosion: a review. Corrosion 2010;66. https://doi.org/10.5006/1.3462912. 075005-075005–075013.

[7] Bermingham MJ, McDonald SD, Dargusch MS, StJohn DH. Grain-refinement mechanisms in titanium alloys. J Mater Res 2008;23:97–104. https://doi.org/10.1557/JMR.2008.0002.

[8] Tamirisakandala S, Miracle DB. Microstructure engineering of titanium alloys via small boron additions. Int J Adv Eng Sci Appl Math 2010;2:168–80. https://doi.org/10.1007/s12572-011-0033-z.

[9] Chao Q, Mateti S, Annasamy M, Imran M, Joseph J, Cai Q, Li LH, Cizek P, Hodgson PD, Chen Y, et al. Nanoparticle-mediated ultra grain refinement and reinforcement in additively manufactured titanium alloys. Addit Manuf 2021;46:102173. https://doi.org/10.1016/j.addma.2021.102173.

[10] Sola A, Trinchi A. Boron-induced microstructural manipulation of titanium and titanium alloys in additive manufacturing. Virtual Phys Prototyp 2023;18:2230467. https://doi.org/10.1080/17452759.2023.2230467.

[11] Hu Y, Ning F, Wang H, Cong W, Zhao B. Laser engineered net shaping of quasi-continuous network microstructural TiB reinforced titanium matrix bulk composites: microstructure and wear performance. Opt Laser Technol 2018;99:174–83. https://doi.org/10.1016/j.optlastec.2017.08.032.

[12] Hu Y, Cong W, Wang X, Li Y, Ning F, Wang H. Laser deposition-additive manufacturing of TiB-Ti composites with novel three-dimensional quasi-continuous network microstructure: effects on strengthening and toughening.

Composites Part B 2018;133:91–100. https://doi.org/10.1016/j.compositesb.2017.09.019.
[13] Minasyan T, Liu L, Aydinyan S, Antonov M, Hussainova I. Selective laser melting of Ti/cBN composite. Key Eng Mater 2019;799:257–62. https://doi.org/10.4028/www.scientific.net/KEM.799.257.
[14] Khorsand Zak A, Abd Majid WH, Abrishami ME, Yousefi R. X-ray analysis of ZnO nanoparticles by Williamson–Hall and size–strain plot methods. Solid State Sci 2011;13:251–6. https://doi.org/10.1016/j.solidstatesciences.2010.11.024.
[15] Ectors D, Goetz-Neunhoeffer F, Neubauer J. A generalized geometric approach to anisotropic peak broadening due to domain morphology. J Appl Crystallogr 2015;48:189–94. https://doi.org/10.1107/S1600576714026557.
[16] Zolotoyabko E. Determination of the degree of preferred orientation within the March–Dollase approach. J Appl Crystallogr 2009;42:513–8. https://doi.org/10.1107/S0021889809013727.
[17] AZtecCrystal - Nanoanalysis [Internet]. Oxf. Instrum [cited 2024 Feb 1]. Available from: https://nano.oxinst.com/aztecrystal.
[18] IFM Facilities - XRay Facility [Internet] Inst. Front. Mater. [cited 2024 Feb 1]. Available from:: https://ifm.deakin.edu.au/facilities/.
[19] XSACT Software [Internet]. Xenocs. [cited 2024 Feb 1]. Available from: https://www.xenocs.com/saxs-products/xsact-software/.
[20] Gureyev TE, Nesterets Y, Ternovski D, Thompson D, Wilkins SW, Stevenson AW, Sakellariou A, Taylor JA. Toolbox for advanced x-ray image processing. Adv Comput Methods X-Ray Opt II. San Diego, CA, USA: SPIE; 2011. p. 81410B, 14 pp.
[21] Avizo Software | Materials Characterization Software - AU [Internet]. [cited 2024 Feb 1]. Available from: https://www.thermofisher.com/au/en/home/electron-microscopy/products/software-em-3d-vis/avizo-software.html.
[22] DebRoy T, Wei HL, Zuback JS, Mukherjee T, Elmer JW, Milewski JO, Beese AM, Wilson-Heid A, De A, Zhang W. Additive manufacturing of metallic components – process, structure and properties. Prog Mater Sci 2018;92:112–224. https://doi.org/10.1016/j.pmatsci.2017.10.001.
[23] Kok Y, Tan XP, Wang P, Nai MLS, Loh NH, Liu E, Tor SB. Anisotropy and heterogeneity of microstructure and mechanical properties in metal additive manufacturing: a critical review. Mater Des 2018;139:565–86. https://doi.org/10.1016/j.matdes.2017.11.021.
[24] Kobryn PA, Semiatin SL. The laser additive manufacture of Ti-6Al-4V. JOM (J Occup Med) 2001;53:40–2. https://doi.org/10.1007/s11837-001-0068-x.
[25] ASTM F2924-14. Specification for additive manufacturing titanium-6 aluminum-4 vanadium with powder bed fusion [internet]. ASTM International; 2021. F42.05 Subcommittee; 2021 [cited 2023 Apr 27]. Available from: http://www.astm.org/cgi-bin/resolver.cgi?F2924-14R21.
[26] Otte JA, Soro N, Yang N, Zou J, Dargusch MS. TiB reinforced lattice structures produced by laser powder bed fusion with high elastic admissible strain. Mater Sci Eng, A 2022;845:143249. https://doi.org/10.1016/j.msea.2022.143249.
[27] Otte JA, Zou J, Dargusch MS. High strength and ductility of titanium matrix composites by nanoscale design in selective laser melting. J Mater Sci Technol 2022;118:114–27. https://doi.org/10.1016/j.jmst.2021.12.020.
[28] Avila JD, Bandyopadhyay A. Influence of boron nitride on reinforcement to improve high temperature oxidation resistance of titanium. J Mater Res 2019;34:1279–89. https://doi.org/10.1557/jmr.2019.11.
[29] Borisova AL, Borisov YuS, Shvedova LK, Martsenyuk IS. Reactions in powder Ti-BN composites. Sov Powder Metall Met Ceram 1984;23:273–6. https://doi.org/10.1007/BF00796385.
[30] Fan Z, Guo ZX, Cantor B. The kinetics and mechanism of interfacial reaction in sigma fibre-reinforced Ti MMCs. Composer Part Appl Sci Manuf 1997;28:131–40. https://doi.org/10.1016/S1359-835X(96)00105-4.
[31] Bhuiyan MMH, Li LH, Wang J, Hodgson P, Chen Y. Interfacial reactions between titanium and boron nitride nanotubes. Scripta Mater 2017;127:108–12. https://doi.org/10.1016/j.scriptamat.2016.09.005.
[32] Chandran KSR, Panda KB. Titanium composites with TiB whiskers. Adv Mater Process 2002;160:59.
[33] Gu DD, Meiners W, Wissenbach K, Poprawe R. Laser additive manufacturing of metallic components: materials, processes and mechanisms. Int Mater Rev 2012;57:133–64. https://doi.org/10.1179/1743280411Y.0000000014.
[34] Wang L, Zhang Z, Zhao Z, Zhang S, Bai P. Mixed grain structure and mechanical property of Ti–6Al–4V–0.5BN (wt%) alloy fabricated by selective laser melting. Acta Metall Sin Engl Lett [Internet] 2023 [cited 2023 Apr 28] 10.1007/s40195-022-01507-2.
[35] Das M, Bhattacharya K, Dittrick SA, Mandal C, Balla VK, Sampath Kumar TS, Bandyopadhyay A, Manna I. In situ synthesized TiB–TiN reinforced Ti6Al4V alloy composite coatings: microstructure, tribological and in-vitro biocompatibility. J Mech Behav Biomed Mater 2014;29:259–71. https://doi.org/10.1016/j.jmbbm.2013.09.006.
[36] Das M, Balla VK, Basu D, Manna I, Sampath Kumar TS, Bandyopadhyay A. Laser processing of in situ synthesized TiB–TiN-reinforced Ti6Al4V alloy coatings. Scripta Mater 2012;66:578–81. https://doi.org/10.1016/j.scriptamat.2012.01.010.
[37] Tamirisakandala S, Miracle DB, Srinivasan R, Gunasekera JS. Titanium alloyed with boron. Adv Mater Process 2006;164 [Internet].
[38] Galvan D, Ocelík V, Pei Y, Kooi BJ, De Hosson JThM, Ramous E. Microstructure and properties of TiB/Ti-6Al-4V coatings produced with laser treatments. J Mater Eng Perform 2004;13:406–12. https://doi.org/10.1361/10599490419919.
[39] Pouzet S, Peyre P, Gorny C, Castelnau O, Baudin T, Brisset F, Colin C, Gadaud P. Additive layer manufacturing of titanium matrix composites using the direct metal deposition laser process. Mater Sci Eng, A 2016;677:171–81. https://doi.org/10.1016/j.msea.2016.09.002.
[40] Hu Y, Zhao B, Ning F, Wang H, Cong W. In-situ ultrafine three-dimensional quasi-continuous network microstructural TiB reinforced titanium matrix composites fabrication using laser engineered net shaping. Mater Lett 2017;195:116–9. https://doi.org/10.1016/j.matlet.2017.02.112.
[41] Singh N, Acharya S, Prashanth KG, Chatterjee K, Suwas S. Ti6Al7Nb-based TiB-reinforced composites by selective laser melting. J Mater Res 2021;36:3691–700. https://doi.org/10.1557/s43578-021-00238-x.
[42] Attar H, Bönisch M, Calin M, Zhang LC, Zhuravleva K, Funk A, Scudino S, Yang C, Eckert J. Comparative study of microstructures and mechanical properties of in situ Ti–TiB composites produced by selective laser melting, powder metallurgy, and casting technologies. J Mater Res 2014;29:1941–50. https://doi.org/10.1557/jmr.2014.122.
[43] Banerjee R, Genç A, Hill D, Collins PC, Fraser HL. Nanoscale TiB precipitates in laser deposited Ti-matrix composites. Scripta Mater 2005;53:1433–7. https://doi.org/10.1016/j.scriptamat.2005.08.014.
[44] Bermingham M, StJohn D, Easton M, Yuan L, Dargusch M. Revealing the mechanisms of grain nucleation and formation during additive manufacturing. JOM (J Occup Med) 2020;72:1065–73. https://doi.org/10.1007/s11837-020-04019-5.
[45] Bermingham MJ, McDonald SD, Dargusch MS. Effect of trace lanthanum hexaboride and boron additions on microstructure, tensile properties and anisotropy of Ti-6Al-4V produced by additive manufacturing. Mater Sci Eng, A 2018;719:1–11. https://doi.org/10.1016/j.msea.2018.02.012.
[46] Xue A, Lin X, Wang L, Wang J, Huang W. Influence of trace boron addition on microstructure, tensile properties and their anisotropy of Ti6Al4V fabricated by laser directed energy deposition. Mater Des 2019;181:107943. https://doi.org/10.1016/j.matdes.2019.107943.
[47] Zhang K, Tian X, Bermingham M, Rao J, Jia Q, Zhu Y, Wu X, Cao S, Huang A. Effects of boron addition on microstructures and mechanical properties of Ti-6Al-4V manufactured by direct laser deposition. Mater Des 2019;184:108191. https://doi.org/10.1016/j.matdes.2019.108191.
[48] Mahbooba Z, West H, Harrysson O, Wojcieszynski A, Dehoff R, Nandwana P, Horn T. Effect of hypoeutectic boron additions on the grain size and mechanical properties of Ti-6Al-4V manufactured with powder bed electron beam additive manufacturing. JOM (J Occup Med) 2017;69:472–8. https://doi.org/10.1007/s11837-016-2210-9.
[49] Patil AS, Hiwarkar VD, Verma PK, Khatirkar RK. Effect of $TiB_2$ addition on the microstructure and wear resistance of Ti-6Al-4V alloy fabricated through direct metal laser sintering (DMLS). J Alloys Compd 2019;777:165–73. https://doi.org/10.1016/j.jallcom.2018.10.308.
[50] Fereiduni E, Ghasemi A, Elbestawi M. Selective laser melting of hybrid ex-situ/in-situ reinforced titanium matrix composites: laser/powder interaction, reinforcement formation mechanism, and non-equilibrium microstructural evolutions. Mater Des 2019;184:108185. https://doi.org/10.1016/j.matdes.2019.108185.
[51] He D, Wang H, Huang W, Chen X, Lian G, Wang Y. Microstructure and mechanical properties of $LaB_6$/Ti-6Al-4V composites fabricated by selective laser melting. Metals 2023;13:264. https://doi.org/10.3390/met13020264.
[52] Essien U, Vaudreuil S. Issues in metal matrix composites fabricated by laser powder bed fusion technique: a review. Adv Eng Mater 2022;24:2200055. https://doi.org/10.1002/adem.202200055.
[53] He Y, Montgomery C, Beuth J, Webler B. Melt pool geometry and microstructure of Ti6Al4V with B additions processed by selective laser melting additive manufacturing. Mater Des 2019;183:108126. https://doi.org/10.1016/j.matdes.2019.108126.
[54] Chua CK, Wong CH, Yeong WY. Ch. 3 - measurement science roadmap for additive manufacturing. In: Chua CK, Wong CH, Yeong WY, editors. Stand qual Control meas sci 3D print addit manuf [internet]. Academic Press; 2017. p. 57–73 [cited 2023 Jun 25], https://www.sciencedirect.com/science/article/pii/B9780128134894000039.
[55] Sola A, Chong WJ, Pejak Simunec D, Li Y, Trinchi A, Kyratzis I, Louis, Wen C. Open challenges in tensile testing of additively manufactured polymers: a literature survey and a case study in fused filament fabrication. Polym Test 2023;117:107859. https://doi.org/10.1016/j.polymertesting.2022.107859.
[56] Sola A, Nouri A. Microstructural porosity in additive manufacturing: the formation and detection of pores in metal parts fabricated by powder bed fusion. J Adv Manuf Process 2019;1:e10021. https://doi.org/10.1002/amp2.10021.
[57] Palmeri D, Buffa G, Pollara G, Fratini L. Sample building orientation effect on porosity and mechanical properties in Selective Laser Melting of Ti6Al4V titanium alloy. Mater Sci Eng, A 2022;830:142306. https://doi.org/10.1016/j.msea.2021.142306.
[58] Wang F, Bosque HD, Hyder J, Corliss M, Hung WN. Experimental investigation of porosity distribution in selective laser melted Inconel 718. Procedia Manuf 2020;48:807–13. https://doi.org/10.1016/j.promfg.2020.05.117.
[59] Stefanescu DM, Ruxanda R. Solidification structures of titanium alloys. In: Vander Voort GF, editor. Metallogr microstruct [internet]. ASM International; 2004. p. 116–26 [cited 2023 Jun 16], http://dl.asminternational.org/handbooks/book/38/chapter/481237/Solidification-Structures-of-Titanium-Alloys.
[60] Tao Q, Wang Z, Chen G, Cai W, Cao P, Zhang C, Ding W, Lu X, Luo T, Qu X, et al. Selective laser melting of CP-Ti to overcome the low cost and high performance trade-off. Addit Manuf 2020;34:101198. https://doi.org/10.1016/j.addma.2020.101198.
[61] Motyka M. Martensite formation and decomposition during traditional and AM processing of two-phase titanium alloys—an overview. Metals 2021;11:481. https://doi.org/10.3390/met11030481.

[62] Oh MS, Lee J-Y, Park JK. Continuous cooling β-to-α transformation behaviors of extra-pure and commercially pure Ti. Metall Mater Trans A 2004;35A:3071–7. https://doi.org/10.1007/s11661-004-0052-5.
[63] Attar H, Calin M, Zhang LC, Scudino S, Eckert J. Manufacture by selective laser melting and mechanical behavior of commercially pure titanium. Mater Sci Eng, A 2014;593:170–7. https://doi.org/10.1016/j.msea.2013.11.038.
[64] Horiuchi Y, Inamura T, Kim HY, Wakashima K, Miyazaki S, Hosoda H. Effect of boron concentration on martensitic transformation temperatures, stress for inducing martensite and slip stress of Ti-24 mol%Nb-3 mol%Al superelastic alloy. Mater Trans 2007;48:407–13. https://doi.org/10.2320/matertrans.48.407.
[65] Bermingham MJ, Kent D, Zhan H, StJohn DH, Dargusch MS. Controlling the microstructure and properties of wire arc additive manufactured Ti–6Al–4V with trace boron additions. Acta Mater 2015;91:289–303. https://doi.org/10.1016/j.actamat.2015.03.035.
[66] Huo J, He B, Lan L. Effects of boron on microstructure and mechanical properties of high-Nb TiAl alloy fabricated via laser melting deposition. J Mater Eng Perform [Internet] 2023. https://doi.org/10.1007/s11665-023-07851-3 [cited 2023 Apr 27].
[67] Williamson GK, Hall WH. X-ray line broadening from filed aluminium and wolfram. Acta Metall 1953;1:22–31. https://doi.org/10.1016/0001-6160(53)90006-6.
[68] Wei S, Zhang Z-H, Wang F-C, Shen X-B, Cai H-N, Lee S-K, Wang L. Effect of Ti content and sintering temperature on the microstructures and mechanical properties of TiB reinforced titanium composites synthesized by SPS process. Mater Sci Eng, A 2013;560:249–55. https://doi.org/10.1016/j.msea.2012.09.064.
[69] Levkulich NC, Semiatin SL, Gockel JE, Middendorf JR, DeWald AT, Klingbeil NW. The effect of process parameters on residual stress evolution and distortion in the laser powder bed fusion of Ti-6Al-4V. Addit Manuf 2019;28:475–84. https://doi.org/10.1016/j.addma.2019.05.015.
[70] Otte JA, Zou J, Huang Y, Dargusch MS. Ultrahigh aspect ratio TiB nanowhisker-reinforced titanium matrix composites as lightweight and low-cost replacements for superalloys. ACS Appl Nano Mater 2020;3:8208–15. https://doi.org/10.1021/acsanm.0c01640.
[71] Izumi F, Ikeda T. Implementation of the Williamson–Hall and halder–wagner methods into RIETAN-FP. Annu Rep Adv Ceram Res Cent Nagoya Inst Technol. 2015;3:33–8.
[72] Germain L, Gey N, Humbert M. Reliability of reconstructed β-orientation maps in titanium alloys. Ultramicroscopy 2007;107:1129–35. https://doi.org/10.1016/j.ultramic.2007.01.012.
[73] Wang SC, Aindow M, Starink MJ. Effect of self-accommodation on α/α boundary populations in pure titanium. Acta Mater 2003;51:2485–503. https://doi.org/10.1016/S1359-6454(03)00035-1.
[74] Yang YF, Yan M, Luo SD, Schaffer GB, Qian M. Modification of the α-Ti laths to near equiaxed α-Ti grains in as-sintered titanium and titanium alloys by a small addition of boron. J Alloys Compd 2013;579:553–7. https://doi.org/10.1016/j.jallcom.2013.07.097.
[75] Zhou Z, Liu Y, Liu X, Zhan Q, Wang K. Microstructure evolution and mechanical properties of in-situ Ti6Al4V–TiB composites manufactured by selective laser melting. Composites Part B 2021;207:108567. https://doi.org/10.1016/j.compositesb.2020.108567.
[76] Cordero ZC, Knight BE, Schuh CA. Six decades of the Hall–Petch effect – a survey of grain-size strengthening studies on pure metals. Int Mater Rev 2016;61:495–512. https://doi.org/10.1080/09506608.2016.1191808.
[77] Guo X, Wang L, Wang M, Qin J, Zhang D, Lu W. Effects of degree of deformation on the microstructure, mechanical properties and texture of hybrid-reinforced titanium matrix composites. Acta Mater 2012;60:2656–67. https://doi.org/10.1016/j.actamat.2012.01.032.
[78] Singh G, Ramamurty U. Boron modified titanium alloys. Prog Mater Sci 2020;111:100653. https://doi.org/10.1016/j.pmatsci.2020.100653.
[79] Li Q, Viereckl A, Rottmair CA, Singer RF. Improved processing of carbon nanotube/magnesium alloy composites. Compos Sci Technol 2009;69:1193–9. https://doi.org/10.1016/j.compscitech.2009.02.020.
[80] Banerjee R, Genç A, Collins PC, Fraser HL. Comparison of microstructural evolution in laser-deposited and arc-melted in-situ Ti-TiB composites. Metall Mater Trans A 2004;35:2143–52. https://doi.org/10.1007/s11661-004-0162-0.
[81] Khajuria G, Wani MF, Mushtaq S, Sehgal R. Optimization of the effect of indentation load and dwell time on micro hardness values using fuzzy logic predictive model. J Phys Conf Ser 2019;1240:012085. https://doi.org/10.1088/1742-6596/1240/1/012085.
[82] Petrík J, Blaško P, Markulík Š, Šolc M, Palfy P. The indentation size effect (ISE) of metals. 2022.
[83] Sen I, Tamirisakandala S, Miracle D, Ramamurty U. Microstructural effects on the mechanical behavior of B-modified Ti–6Al–4V alloys. Acta Mater 2007;55:4983–93. https://doi.org/10.1016/j.actamat.2007.05.009.
[84] Tamirisakandala S, Bhat RB, Tiley JS, Miracle DB. Grain refinement of cast titanium alloys via trace boron addition. Scripta Mater 2005;53:1421–6. https://doi.org/10.1016/j.scriptamat.2005.08.020.
[85] Xia M, Liu A, Hou Z, Li N, Chen Z, Ding H. Microstructure growth behavior and its evolution mechanism during laser additive manufacture of in-situ reinforced (TiB+TiC)/Ti composite. J Alloys Compd 2017;728:436–44. https://doi.org/10.1016/j.jallcom.2017.09.033.
[86] Han C, Babicheva R, Chua JDQ, Ramamurty U, Tor SB, Sun C-N, Zhou K. Microstructure and mechanical properties of (TiB+TiC)/Ti composites fabricated in situ via selective laser melting of Ti and B4C powders. Addit Manuf 2020;36:101466. https://doi.org/10.1016/j.addma.2020.101466.
[87] Fischer-Cripps AC. Analysis of instrumented indentation test data for functionally graded materials. Surf Coat Technol 2003;168:136–41. https://doi.org/10.1016/S0257-8972(03)00015-X.
[88] Giannakopoulos AE, Larsson P-L, Vestergaard R. Analysis of Vickers indentation. Int J Solid Struct 1994;31:2679–708. https://doi.org/10.1016/0020-7683(94)90225-9.
[89] Murakami Y, Matsuda K. Analysis of Vickers hardness by the finite element method. J Appl Mech 1994;61:822–8. https://doi.org/10.1115/1.2901563.
[90] Zhao Y, Gu Y, Guo Y. Plasticity and deformation mechanisms of ultrafine-grained Ti in necking region revealed by digital image correlation technique. Nanomaterials 2021;11:574. https://doi.org/10.3390/nano11030574.
[91] Dongare S, Sparks TE, Newkirk J, Liou F. A mechanical testing methodology for metal additive manufacturing processes. University of Texas at Austin; 2014 [cited 2023 Jun 27]. Available from: https://repositories.lib.utexas.edu/handle/2152/88745.
[92] Crocker L. Literature review on tensile test standards for metal additive manufacturing [Internet]. Hampton Road, Teddington, Middlesex, TW11 0LW. National Physical Laboratory; 2019 [cited 2024 Aug 18]. p. 16. Report No.: NPL Report MAT 89. Available from: https://eprintspublications.npl.co.uk/8508/1/MAT89.pdf.
[93] Jia D, Wang YM, Ramesh KT, Ma E, Zhu YT, Valiev RZ. Deformation behavior and plastic instabilities of ultrafine-grained titanium. Appl Phys Lett 2001;79:611–3. https://doi.org/10.1063/1.1384000.
[94] Attar H, Bönisch M, Calin M, Zhang L-C, Scudino S, Eckert J. Selective laser melting of in situ titanium–titanium boride composites: processing, microstructure and mechanical properties. Acta Mater 2014;76:13–22. https://doi.org/10.1016/j.actamat.2014.05.022.
[95] Dong Y, Li Y, Ebel T, Yan M. Cost-affordable, high-performance Ti–TiB composite for selective laser melting additive manufacturing. J Mater Res 2020;35:1922–35. https://doi.org/10.1557/jmr.2019.389.
[96] Huang D, Zhou Y, Yao X, Tan Q, Chang H, Wang D, Lu S, Liu S, Xu J, Jin S, et al. From crack-prone to crack-free: unravelling the roles of $LaB_6$ in a β-solidifying TiAl alloy fabricated with laser additive manufacturing. Mater Sci Eng, A 2022;861:144358. https://doi.org/10.1016/j.msea.2022.144358.
[97] Voisin T, Calta NP, Khairallah SA, Forien J-B, Balogh L, Cunningham RW, Rollett AD, Wang YM. Defects-dictated tensile properties of selective laser melted Ti-6Al-4V. Mater Des 2018;158:113–26. https://doi.org/10.1016/j.matdes.2018.08.004.
[98] Hrabe N, Barbosa N, Daniewicz S, Shamsaei N. Findings from the NIST/ASTM workshop on mechanical behavior of additive manufacturing components. Gaithersburg, MD: National Institute of Standards and Technology; 2016 [cited 2023 Jun 15]. pp. 1–256. Report No.: NIST Advanced Manufacturing Series 100-4. Available from: https://nvlpubs.nist.gov/nistpubs/ams/NIST.AMS.100-4.pdf.
[99] Johns-Rahnejat PM, Dolatabadi N, Rahnejat H. Elastic and elastoplastic contact mechanics of concentrated coated contacts. Lubricants 2024;12. https://doi.org/10.3390/lubricants12050162.
[100] Herzog T, Brandt M, Trinchi A, Sola A, Hagenlocher C, Molotnikov A. Defect detection by multi-axis infrared process monitoring of laser beam directed energy deposition. Sci Rep 2024;14:3861. https://doi.org/10.1038/s41598-024-53931-2.
[101] Trinchi A, Sola A. Embedding function within additively manufactured parts: materials challenges and opportunities. Adv Eng Mater 2023;25:2300395. https://doi.org/10.1002/adem.202300395.
[102] Sola A, Trinchi A, Hill AJ. Self-assembly meets additive manufacturing: bridging the gap between nanoscale arrangement of matter and macroscale fabrication. Smart Mater Manuf 2023;1:100013. https://doi.org/10.1016/j.smmf.2022.100013.